

Dynamic Realtime z-Shimming: A Feasibility Study

E. Alonso-Ortiz¹, A. D'Astous¹, D. Papp¹, J. Cohen-Adad^{1,2,3}

¹*NeuroPoly Lab, Electrical Engineering department, Polytechnique Montréal, QC, Canada*

²*Functional Neuroimaging Unit, CRIUGM, Université de Montréal, Montréal, QC, Canada*

³*Mila - Quebec AI Institute, Montréal, QC, Canada*

Abstract

Respiration causes time-varying frequency offsets that can result in ghosting artifacts. We propose a solution, which we term *dynamic realtime z-shimming*, wherein linear gradients are adjusted dynamically (slice-wise) and in real-time, to reflect magnetic field inhomogeneities that arise during image acquisition. In dynamic z-shimming, a method that is commonly used to reduce static frequency offsets in MR images of the spinal cord and brain, in-plane (static) frequency offsets are assumed to be homogeneous. Here we investigate whether or not that same assumption can be made for time-varying frequency offsets in the cervical spinal cord region. In order to explore the feasibility of *dynamic realtime z-shimming*, we acquired images using a pneumatic phantom setup, as well as in-vivo. We then simulated the effects of time-varying frequency offsets on MR images acquired with and without *dynamic realtime z-shimming* in different scenarios. We found that *dynamic realtime z-shimming* can reduce ghosting if the time-varying frequency offsets have an in-plane variability (standard deviation) of $\lesssim 1$ Hz. This scenario was achieved in our phantom setup, where we observed a 50.2% reduction in ghosting within multi-echo gradient echo images acquired with *dynamic realtime z-shimming*, compared to without. On the other hand, we observed that the in-plane variability of the time-varying frequency offsets is too high within the cervical spinal cord region for *dynamic realtime z-shimming* to be successful. These results can serve as a guideline and starting point for future *dynamic realtime z-shimming* experiments in which the in-plane variability of frequency offsets are minimized.

Introduction

An important challenge for spinal cord (SC) and brain imaging is proximity of the tissues of interest to air in the lungs, cartilage and bone. The different magnetic susceptibility (χ) between soft tissues in the brain and SC and these surrounding structures leads to macroscopic (greater than the voxel dimensions) static field inhomogeneities (ΔB_0), which can result in signal loss in T_2^* -weighted images (1) and geometric distortions in echo-planar imaging (EPI) (2). Further compounding this issue is the fact that during respiration, the volume of air in the lungs changes, leading to time-varying ΔB_0 . Time-varying ΔB_0 causes mislocalization of signals, which manifests as ghosting along the phase-encoding direction.

Static ΔB_0 can be minimized by active shimming; generating compensatory magnetic fields with approximately the same spatial distribution and magnitude, but opposite sign, as that of ΔB_0 . Shimming is commonly achieved by measuring ΔB_0 , and subsequently decomposing the ΔB_0 distribution into a set of spherical harmonic basis functions. Three first order spherical harmonic terms describe linear deviations from a uniform field, corrected using linear gradient coils. The five second order spherical harmonic terms describe quadratic deviations from a uniform field, which are generated using a combination of the linear gradient coils and additional second order coils in clinical/typical scanners (3). However, in areas of strong, localized ΔB_0 , such as the SC region, the prefrontal cortex or the medial temporal lobe, severe residual inhomogeneities remain after conventional shimming (1). To address this issue, a number of solutions have been proposed, such as higher-order spherical harmonic insert coils (4), external multi-coil arrays that produce non-orthogonal field patterns (5,6), or “dynamic shimming”, whereby spherical harmonic shims can be optimized on a slice-by-slice basis (6,7).

MRI of the SC often necessitates high in-plane resolution, due to the small dimensions of the SC structures, and thick slices, to maintain an adequate signal-to-noise (SNR) ratio. Consequently, sensitivity to ΔB_0 has often been considered to be highest along the slice-select direction. In order to reduce the effects of high ΔB_0 along the slice-select direction, a technique called “z-shimming” has been used for brain MRI. z-Shimming seeks to reduce through-slice signal dephasing in T_2^* -

weighted acquisitions by applying slice-specific linear compensation gradients along the slice-select axis (8). For small regions-of-interest (ROIs), such as the cervical SC, wherein ΔB_0 does not vary considerably in-plane, z-shimming has been successfully employed using single slice-specific compensation gradients (1). However, z-shimming does not compensate for time-varying effects.

In order to mitigate the effects of time-varying ΔB_0 , a number of solutions have been proposed, such as, navigator echoes (9,10), retrospective correction methods (11,12) or real-time (i.e. “realtime”) control shimming. The latter has been demonstrated in the brain at 7 T by monitoring respiration through the use of respiratory bellows and adjusting the scanner’s 1st and 2nd order spherical harmonic shims in real-time (13). In (13), hardware modifications were made so that the shims could be run independently of the scanner. More recently, realtime shimming was achieved in the SC using a custom-built shim coil (14). While the prospective nature of realtime shimming is attractive, its reliance on specialized hardware limits its widespread adoption.

In this work, we investigate a solution for the time-varying component of ΔB_0 in which the scanner’s first order shim coils are used to create compensation gradients along the slice-select (“z”) direction. These z-shimming gradients are updated dynamically (slice-wise) and in real-time to reflect respiration-induced changes in ΔB_0 . The approach does not require hardware modifications, or specialized coils.

We refer to this technique as *dynamic realtime z-shimming* (dRTz-shim). Through simulations, we show that dRTz-shim requires high in-plane uniformity of the time-varying component of ΔB_0 and that this cannot be assumed for full field-of-view, conventional, cervical SC imaging. In order to demonstrate this using real MR data, we implemented dRTz-shim in a multi-echo gradient-echo (MGRE) sequence. We then acquired images at 3 T using a phantom setup consisting of a pneumatic device, used to generate a time-varying ΔB_0 , and a small mineral oil-filled test tube, as well as in a human volunteer. The phantom data illustrates the conditions under which dRTz-shim can reduce artifacts due to time-varying ΔB_0 and the in-vivo data supports our simulations, which suggest that, unlike static ΔB_0 , time-varying ΔB_0 in the cervical SC region are not sufficiently uniform within the imaging plane for dRTz-shim to be effective at reducing artifacts.

Theory

The effects of time-varying ΔB_0 on the measured signal

We assume that during normal breathing, the magnetic field at every point in space varies sinusoidally in time and oscillates about an equilibrium value ($\Delta B_{static}(r)$) with an angular frequency ω_{resp} (12,14). We do not expect this assumption to hold during breath-hold experiments, or in other irregular breathing scenarios. Hereafter, values of ΔB_0 are considered to be in units of Hz, following common convention.

$$\Delta B_0(r, t) = \Delta B_{static}(r) + RIRO_{max}(r) \sin(\omega_{resp} t), \quad [1]$$

where $RIRO_{max}$ is the maximum respiration-induced resonance offset. The focus of this work is not the effect of $\Delta B_{static}(r)$, but rather that of respiration-induced resonance offsets ($RIRO(r) = RIRO_{max}(r) \sin(\omega_{resp} t)$). For this reason, we will presume that the static component of the magnetic field offset is relatively uniform in-plane ($\Delta B_{static}(r) \cong \Delta B_{static}(z)$) (1), whereas the respiration-induced offsets are not; $RIRO_{max}(r) = RIRO_{max}(x, y, z)$.

For a 2D experiment, the (demodulated) signal measured at TE , within a given slice z , will be:

$$\begin{aligned} S(TE) &= \iint \rho(x, y) e^{-i2\pi(k_x x + k_y y) - i2\pi \Delta B_0(x, y, t) \cdot TE} dx dy \\ &= e^{-i2\pi \Delta B_{static} \cdot TE} \iint \rho(x, y) e^{-i2\pi(k_x x + k_y y) - i2\pi RIRO_{max}(x, y) \sin(\omega_{resp} t) \cdot TE} dx dy, \quad [2] \end{aligned}$$

where t is the time since the start of the experiment, ΔB_{static} is the uniform static resonance offset for the slice in question and $RIRO_{max}(x, y) \sin(\omega_{resp} t)$ is the non-uniform respiration-induced resonance offset distribution in that slice. t can be replaced by $t' + TE$, where t' is the time elapsed from the application of the first phase-encoding step to the current phase encoding step. t' can be expressed in the following terms (15):

$$t' = \left(\frac{G_y}{\Delta G_y} + \frac{n_y}{2} \right) \cdot TR = \left(\frac{k_y}{\Delta k_y} + \frac{n_y}{2} \right) \cdot TR, \quad [3]$$

where the first phase encoding step is $-n_y/2 = G_y/\Delta G_y$.

The measured signal is now equal to:

$$S(TE) = e^{-i2\pi\Delta B_{static}\cdot TE} \int \int \rho(x, y) e^{-i2\pi(k_x x + k_y y) - i2\pi RIR_{Omax}(x, y) \sin\left(\omega_{resp}\left(\left(\frac{k_y}{\Delta k_y} + \frac{n_y}{2}\right)TR + TE\right)\right)} \cdot TE dx dy. \quad [4]$$

The term outside of the integral in Equation 4 will lead to signal loss via spin dephasing, whereas the sinusoidal term inside the integral will contribute to image replication along the phase-encode (k_y) direction (ghosting artifacts) (16).

If the respiration-induced resonant offset does not vary considerably in-plane, the two aforementioned unwanted signal contributions can be minimized by including compensation gradients, along the slice-select (z) direction, in the pulse sequence used for image acquisition. Figure 2 shows a modified MGRE sequence (panel C) in which each echo is preceded by slice-specific compensation gradients along the z -axis ($G_{z,corr}$).

The moment (amplitude · duration) of $G_{z,corr}$ should be equal to:

$$- \langle G_z \rangle \cdot TE, \quad [5]$$

where $\langle G_z \rangle$ represents the gradient of the magnetic field along the slice-select axis, averaged across the specific slice in question, at time t' :

$$\langle G_z \rangle = \langle G_z(x, y, t') \rangle_{(x, y)}. \quad [6]$$

Methods

Mechanical Phantom and Imaging Experiment

We adapted a mechanical phantom (17) to simulate time-varying ΔB_0 induced by breathing. An air compressor (located in the equipment room) was used to drive two sticks back-and-forth with a period of approximately 2.5 s, close to that of human respiration. A small ferromagnetic object

(a staple) was attached to the end of the first stick, which was placed at the edge of a test tube (1.5 cm in diameter) filled with mineral oil. The tip of the second stick was placed such that it would push against respiratory bellows that had been taped onto a large, heavy phantom, in an oscillatory fashion (Figure 1). The respiratory bellows were connected to Siemens' physiological monitoring unit (PMU) system, which consists of a transmitter unit that sends the pressure signal, sampled at 50 Hz, to the scanner. The test tube was scanned using a 4-channel small flexible coil on a 3 T Prisma MRI scanner (Siemens Healthineer, Erlangen, Germany).

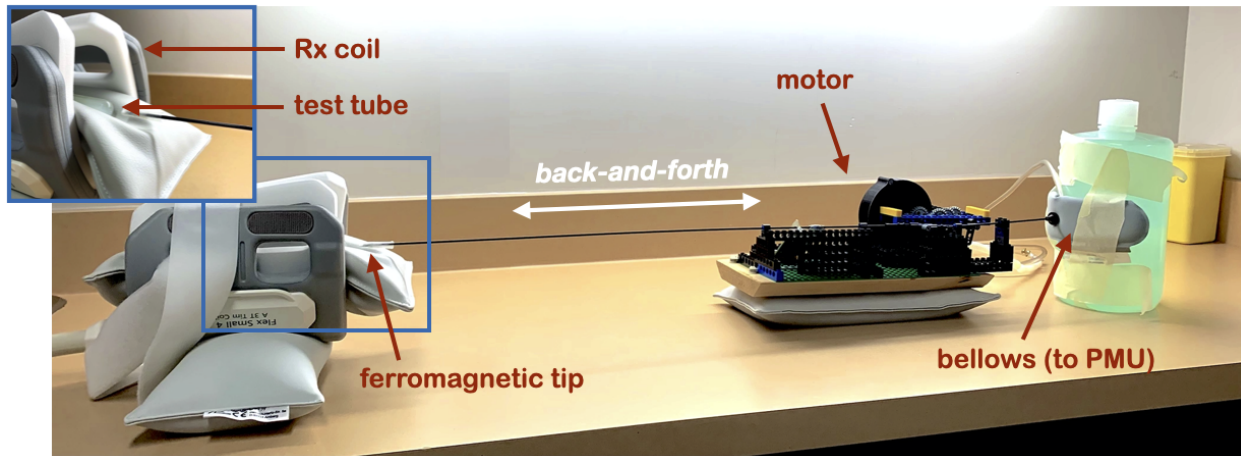


Figure 1: Pneumatic phantom setup. An air compressor blows on a fan, the rotation motion is converted to a sine-like translational motion via a Lego-based system. A long stick presses on a respiratory bellow on one end of the stick while the other end has a small ferromagnetic tip attached to it and is located close to the test tube to be imaged.

In order to determine the appropriate slice-specific compensation gradients ($G_{z,corr}$), the relationship between the measured pressure ($P(t)$) and the magnetic field gradient along z ($G_z(x,y,z)$) must be determined:

$$G_z(x, y, t) = G_{z,static}(x, y) + RIGO_{z,max}(x, y) \cdot P(t), \quad [7]$$

where $RIGO_{z,max}(x,y)$ is the maximum respiration-induced z -gradient offset. This is achieved during a “Training Session”, as illustrated in Figure 2 (panels A and B).

Training Session (Figure 2, panel A):

The scanner's shim volume was manually set to cover the test tube for standard (static) shimming. 60 sequential, sagittal ΔB_0 maps were first acquired along the midline of the test tube, using a dual-echo field mapping sequence (TR = 21 ms, TE₁ = 2.46 ms, TE₂ = 4.92 ms, BW = 900 Hz/pixel, FA = 20⁰, matrix = 96 x 40, image resolution = 1.25 x 1.25 mm², 3 contiguous slices of 2.4 mm thickness). At the start of the field map series the PMU signals read into the scanner were automatically written to a log file, along with the log file start and stop times. The scanner's shim adjustment volume and the shim values used for ΔB_0 mapping were kept constant throughout all the scans that were subsequently acquired. An axial MGRE scan was acquired (8 echoes with 3 ms inter-echo spacing, TE₁ = 2.5 ms, BW = 600 Hz/px, 13 slices contiguous slices of 3 mm thickness, matrix = 128 x 56, image resolution = 2.2 x 2.2 mm², FA = 20⁰) with a long repetition time (TR = 1000 ms) in order to maximize the ghosting artifacts (Equation 4). All the data were conveniently transferred to a laptop via an ethernet socket.

In-vivo scans were also acquired in a healthy human participant on the same 3 T scanner using a 64-channel head-neck coil. Informed consent was given prior to the scanning session (study approved by the Comité d'éthique de la recherche du Regroupement Neuroimagerie Québec). Respiratory bellows were strapped to the volunteer's chest and connected to the PMU. The scanner's shim volume was manually set to cover the area of interest in the spinal cord. 60 sequential, sagittal field maps were first acquired along the midline of the spinal cord, using a dual-echo field mapping sequence (TR = 21 ms, TE₁ = 2.46 ms, TE₂ = 4.92 ms, matrix = 96 x 80, image resolution = 3 x 3 mm², 3 slices with 3.6 mm slice thickness, FA = 20⁰). The scanner's shim adjustment volume and the shim values used for ΔB_0 mapping were kept constant throughout all the scans that were subsequently acquired. The axial MGRE scan was then acquired (TR = 1000 ms, 8 echoes with 3 ms inter-echo spacing, TE₁ = 2.5 ms, BW = 600 Hz/px, 20 slices contiguous slices of 3 mm thickness, matrix = 128 x 84, image resolution = 2.3 x 2.3 mm², FA = 25⁰) with the central slice oriented perpendicularly to the spinal cord at C6/C7.

Data Analysis (Figure 2, panel B):

The time stamps in the PMU log file were used to associate the pressure readings with the ΔB_0 map acquisition times, which were recorded in the header of the image files. Then, using the shimming-toolbox (18), the gradient along the z-axis for each ΔB_0 map in the time series was computed and a linear regression between the gradient and the measured pressure was performed for each voxel (Equation 7). The resulting $G_{z,static}$ and $RIGO_{z,max}$ images were resampled and registered to the target MGRE scan and the average values within an ROI for each slice in the MGRE scan were written into a text file ($\langle G_{z,static} \rangle_{ROI}$ and $\langle RIGO_{z,max} \rangle_{ROI}$) and transferred to the MRI scanner's computer system. For in-vivo scans, the ROI was obtained by generating a mask around the SC using the spinal cord toolbox (SCT) (19).

Dynamic Realtime z-Shimming (dRTz-shim) (Figure 2, panel C):

2D MGRE images were acquired using the same protocol as the first axial MGRE scan (with the same slice positioning, shim adjustment volume and scanner shim gradient values) but with dRTz-shim (Figure 2, panel C) activated. The $\langle G_{z,static} \rangle_{ROI}$ and $\langle RIGO_{z,max} \rangle_{ROI}$ values for each slice were read by the sequence at the start of the acquisition and the pressure on the bellows was continuously sampled by the scanner at a rate of 50 Hz. Before exciting each slice, the sequence retrieves the bellows' pressure, so that the average gradient of the magnetic field along the z-axis, for that slice, can be predicted:

$$\langle G_z \rangle = \langle G_{z,static} \rangle_{ROI} + \langle RIGO_{z,max} \rangle_{ROI} \cdot P(t') \quad [8]$$

Finally, using Equation 5, the appropriate compensation gradient was computed.

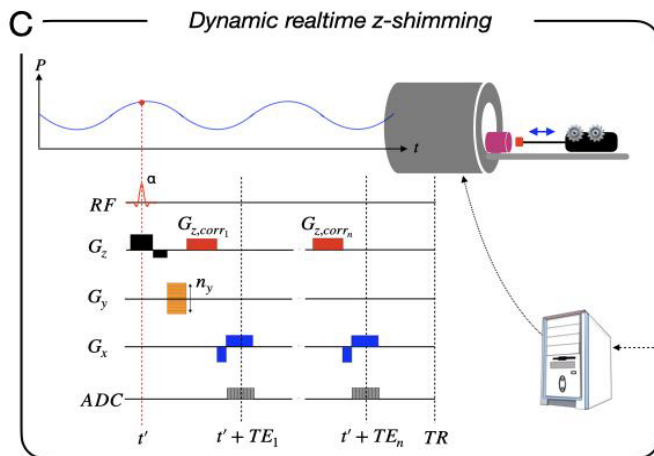
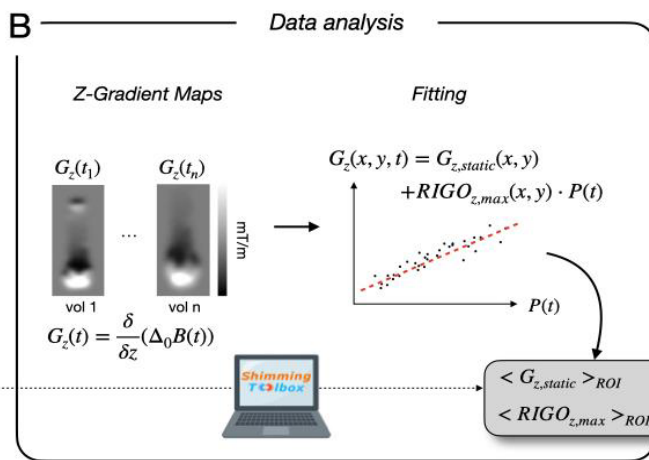
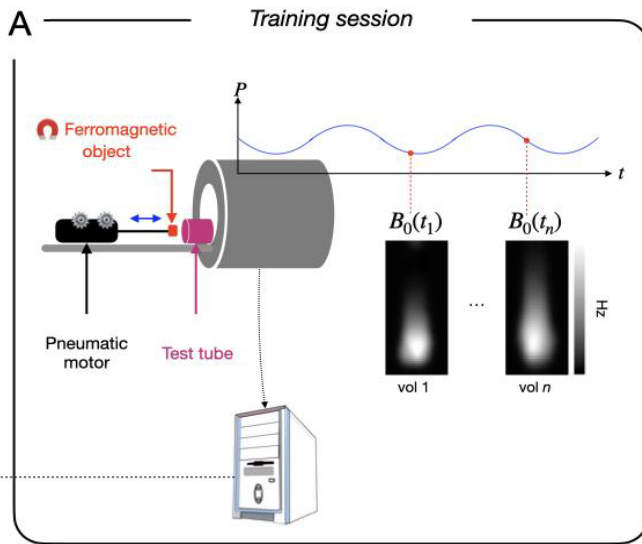


Figure 2: (A) Pneumatic phantom setup with pressure readings obtained from bellows and a time series of ΔB_0 maps. (B) G_z map time series and an illustration of voxel wise linear regression of $G_z(x,y)$ vs. pressure readings. The transfer of slice-specific compensation gradient data ($\langle G_{z,static} \rangle_{ROI}$ and $\langle RIGO_{z,max} \rangle_{ROI}$) is illustrated. (C) dRTz-shim acquisition with a modified MGRE sequence and realtime monitoring of pressure readings.

Post-processing

In order to quantify ghosting, we computed the Percent Signal Ghosting (PSG) (20) on the MGRE phantom images with and without dRTz-shim:

$$PSG = 100 \times \left| \frac{(\text{above} + \text{below})}{2 \times \text{phantom}} \right|, \quad [9]$$

where “above”, “below” and “phantom” refer to ROIs above, below and within the phantom, as indicated in Supplementary Figure S1.

For in-vivo scans, a background mask was manually generated from MGRE images, such that the signal above and below (Equation 9) could be replaced by the mean background signal and the signal in denominator of Equation 9 could be replaced by the mean signal within the SC ROI described in Data Analysis section.

Simulations

To demonstrate the effects of dRTz-shim we simulated two scenarios, one in which the $RIRO_{max}$ distribution had an in-plane variability close to that which was observed in-vivo (“in-vivo simulation”), and another wherein the in-plane variability of $RIRO_{max}$ was more representative of what was measured in our phantom setup (“phantom simulation”). To do this, we first performed a linear regression between the ΔB_0 map time series and the measured pressure readings, resulting in ΔB_{static} and $RIRO_{max}$ images. The latter were resampled and registered to the target MGRE scans (for both in-vivo and phantom datasets). For the in-vivo scan, the spinal cord was segmented on the MGRE scan, using SCT (19). Next, the standard deviation of the

resampled $RIRO_{max}$ images was computed within the imaged object as well as within the spinal cord ROI (for the in-vivo scan).

In-Vivo Simulation:

We used a single axial slice of an MPRAGE T1w scan (matrix = 256 x 256, resolution = 0.9 x 0.9 mm²) covering the cervical SC for our simulations. SCT (19) was used to create an ROI covering the SC. We defined a spatial distribution for $RIRO_{max}$ in which respiration leads to $RIRO_{max} = 12$ Hz at a point in the center of the object and decreases radially, such that the in-plane standard deviation of $RIRO_{max}$ within the simulated object was 2.1 Hz, closely matching that which was measured in-vivo.

Using Equation 2, an expression was derived for the measured signal when using slice-specific compensation gradients along the z-axis ($G_{z,corr}$):

$$S(t) = \int \int \rho(x, y) e^{-2\pi i(k_x x + k_y y) - i2\pi \Delta B_0(x, y, t) \cdot t - i2\pi \Delta B_{0,corr}(t') \cdot t} dx dy, \quad [10]$$

where

$$\Delta B_{0,corr}(t') = \Delta B_{static,corr} + RIRO_{max,corr} \sin(\omega_{resp} t'). \quad [11]$$

t' is the time at which the RF pulse is applied (see Figure 2). If we substitute Equations 1 and 3 in Equation 10:

$$S(TE) = e^{-i2\pi(\Delta B_{static} - \Delta B_{static,corr}) \cdot TE} \int \int \rho(x, y) e^{-i2\pi(k_x x + k_y y)} \cdot e^{-i2\pi \left(RIRO_{max}(x, y) \cdot \sin\left(\omega_{resp} \left(\left(\frac{k_y}{\Delta k_y} + \frac{n_y}{2}\right) \cdot TR + TE\right)\right) - RIRO_{max,corr} \cdot \sin\left(\omega_{resp} \left(\frac{k_y}{\Delta k_y} + \frac{n_y}{2}\right) \cdot TR\right) \right) \cdot TE} dx dy. \quad [12]$$

We will assume that $\Delta B_{static} \cong \Delta B_{static,corr}$ (that is, we are effectively recovering the signal loss that occurs due to static field inhomogeneities), so we omit this term in our simulations. The goal of dRTz-shim is to minimize the difference between the two terms in the latter exponential.

To simulate Equation 12, we set the period of respiration to 3 s, TR = 1000 ms and TE = 15 ms. $RIRO_{max,corr}$ was set to be equal to the average $RIRO_{max}$ in the SC ROI.

Phantom Simulation:

A single slice (matrix = 128 x 56, resolution = 2.2 x 2.2 mm²) was simulated with a cylinder of 10 mm radius. We defined a spatial distribution for $RIRO_{max}$ in which respiration leads to $RIRO_{max} = 12$ Hz at a point in the center of the object and decreases radially, such that the in-plane standard deviation of $RIRO_{max}$ within the simulated object was 1.2 Hz, closely matching that which was measured in-vivo. Equation 12 was used to simulate dRTz-shim, using a period of oscillation equal to 3 s, TR = 1000 ms and TE = 15 ms. $RIRO_{max,corr}$ was set to be equal to the average $RIRO_{max}$ measured in the cylindrical object.

Results

Imaging

In Figure 3 we show the PSG measured in MGRE phantom images without (blue) and with (orange) dRTz-shim for each slice and echo time. Note that in both conditions, the same standard volumetric static shimming was run, so the only difference between these two conditions is the presence/absence of dRTz-shim. The SNR of images acquired without dRTz-shim is reported alongside PSG in Figure 3 so that PSG in images with a high noise level can be contextualized. When considering the PSG averaged across echoes and slices, dRTz-shim led to a 50.2% decrease in PSG.

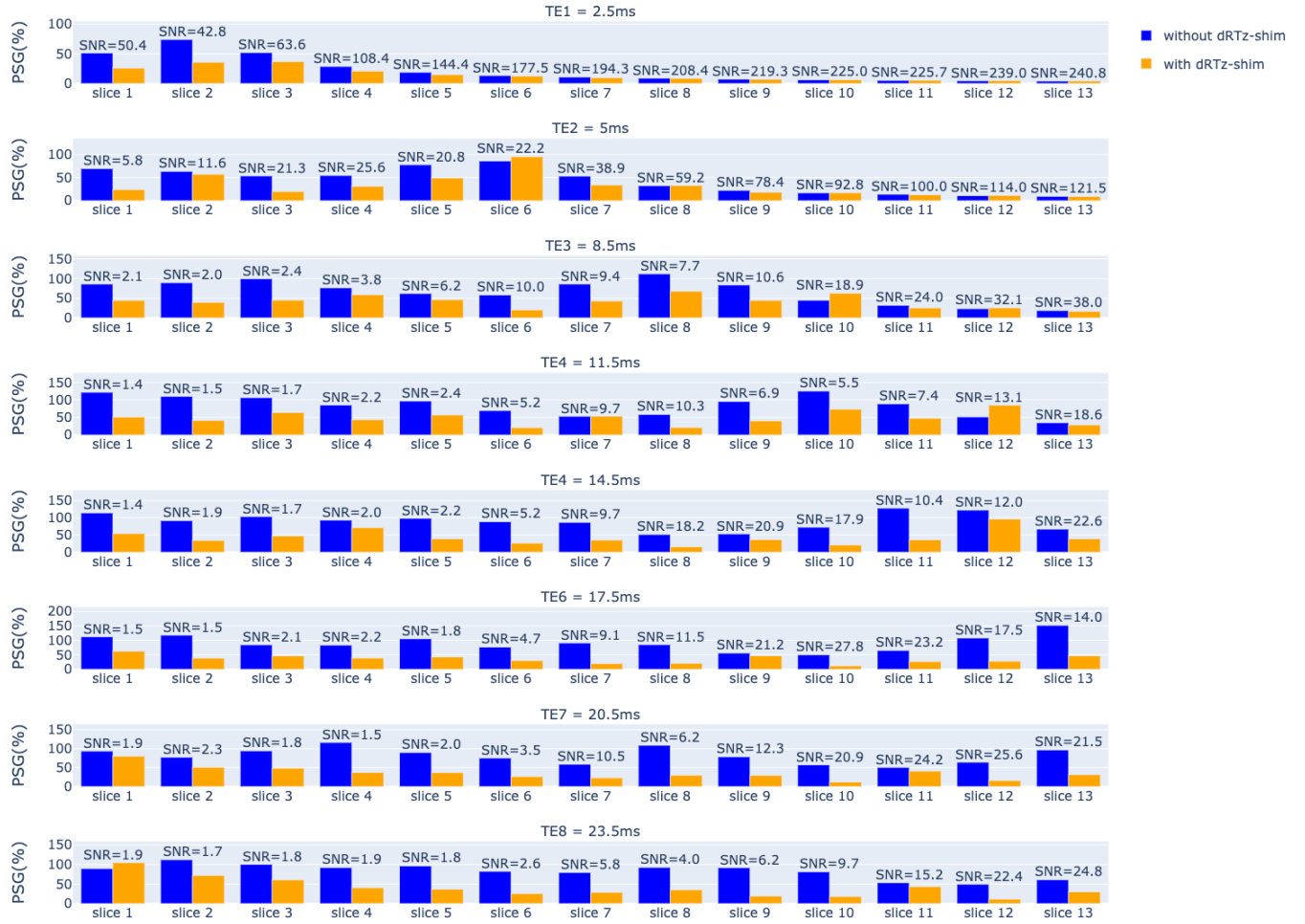


Figure 3: Percent signal ghosting for each echo and slice in MGRE images acquired in a mineral oil-filled phantom without (blue) and with (orange) dRTz-shim. Slice 1 is closest to the paramagnetic material.

Figure 4 shows the PSG averaged across all slices, for each echo time, measured in-vivo without (blue) and with (orange) dRTz-shim. The mean SNR measured across slices for each echo time in images without dRTz-shim is reported alongside the PSG. When considering the PSG averaged across echoes and slices, dRTz-shim led to 11.5(4.6)% PSG, compared to 10.9(3.9)% PSG without dRTz-shim (standard deviation reported in the brackets).

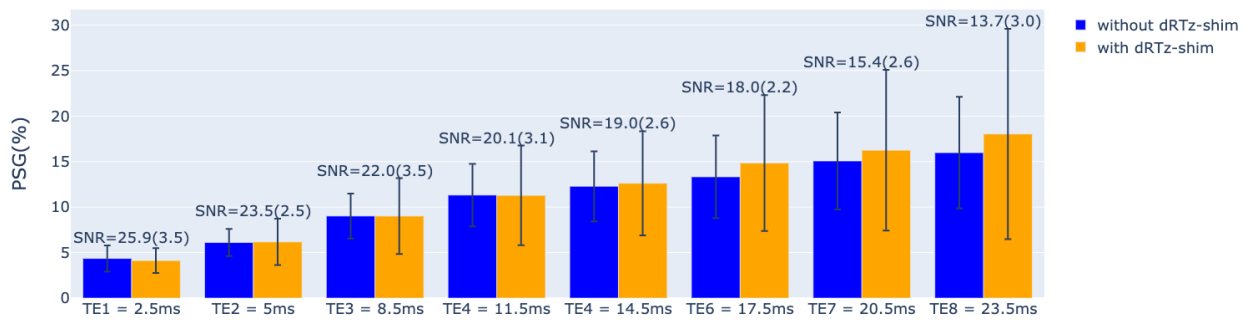


Figure 4: Percent signal ghosting averaged across all slices for each echo in MGRE images acquired in-vivo without (blue) and with (orange) dRTz-shim.

Representative images for our MGRE scans acquired in a phantom are shown in Figure 5 (panel A). On the top row, we see severe ghosting for images acquired without dRTz-shim. On the bottom row we see how dRTz-shim leads to both signal recovery and a reduction in ghosting. In the in-vivo images (Figure 5, panel B), one can appreciate how dRTz-shim results in images in which ghosting persists.

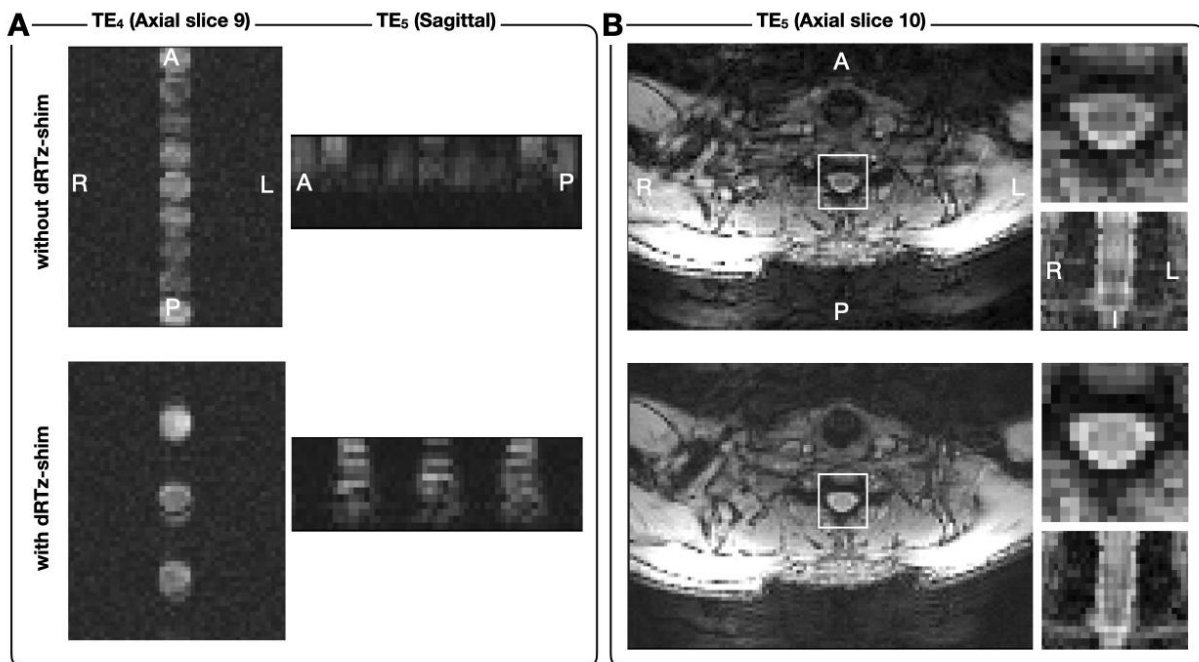


Figure 5: (A) MGRE images acquired in a mineral oil-filled phantom without (top) and with (bottom) dRTz-shim. (B) MGRE images acquired in-vivo without (top) and with (bottom) dRTz-shim. Image scaling is the same between the two conditions. A: Anterior, P: Posterior, R: Right, L: Left.

The in-plane standard deviation of the resampled $RIRO_{max}$ images is shown in Figure 6 across all slices in the phantom scan (blue), in-vivo scan (red), and within the SC ROI for the in-vivo scan (green). Barring the first few slices which were closest to the ferromagnetic object, the phantom scan resulted in an in-plane $RIRO_{max}$ variation that was close to that of the SC ROI. This indicates that our phantom setup leads to an in-plane $RIRO_{max}$ variation that is similar to that of the SC region.

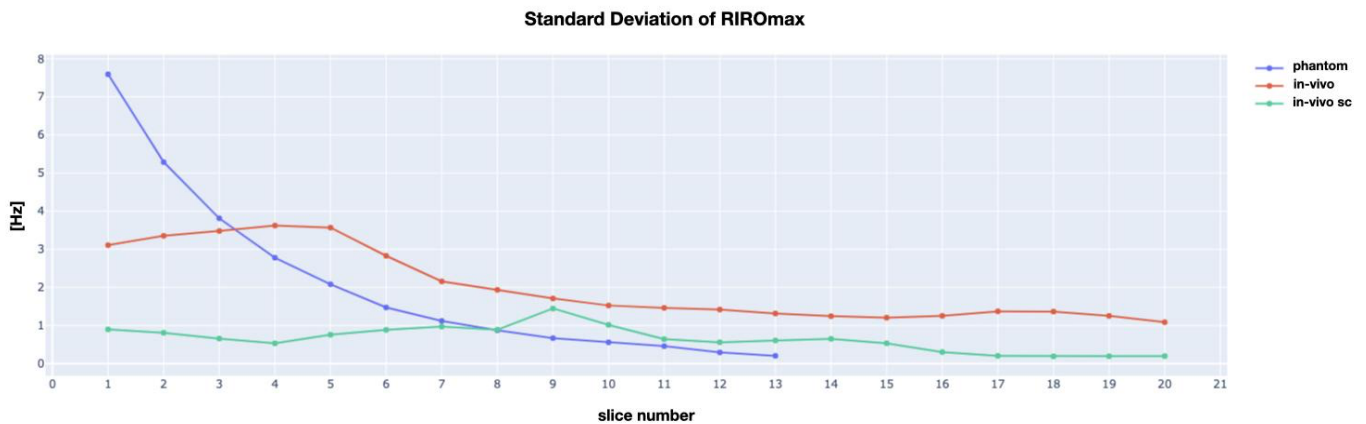


Figure 6: In-plane standard deviation of $RIRO_{max}$ across all slices for a phantom (blue), in-vivo scan (red), and in-vivo SC ROI (green).

Simulations

In Figure 7 we show the T1w scan with the corresponding slice that was used for simulations (A) the simulated $RIRO_{max}$ distribution (B), the simulated measurement (without dRTz-shim) and the simulated dRTz-shim measurement (C). Here we see that with the in-plane variation of $RIRO_{max}$ that one observes in-vivo, ghosting persists when dRTz-shim is simulated, as was observed in our in-vivo scans (Figure 5, panel B).

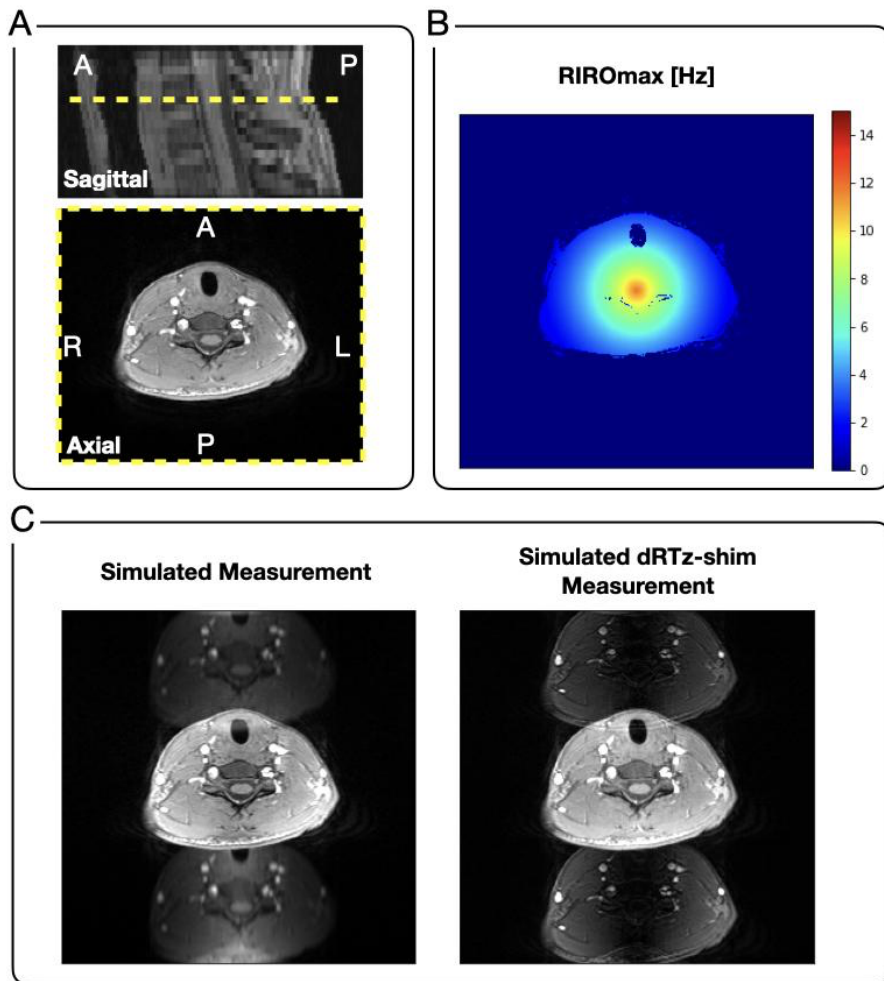


Figure 7: (A) T1w scan with the axial slice that was used in simulations (B) Simulated $RIRO_{max}$ distribution (C) Simulated measurements without and with dRTz-shim. A: Anterior, P: Posterior, R: Right, L: Left.

In Figure 8 we show the simulated cylindrical phantom scan (A), the simulated $RIRO_{max}$ distribution (B), the simulated measurement (without dRTz-shim) and the simulated dRTz-shim measurement (C). Here we observe that the in-plane $RIRO_{max}$ variation is small enough for dRTz-shim to lead to an improvement in ghosting.

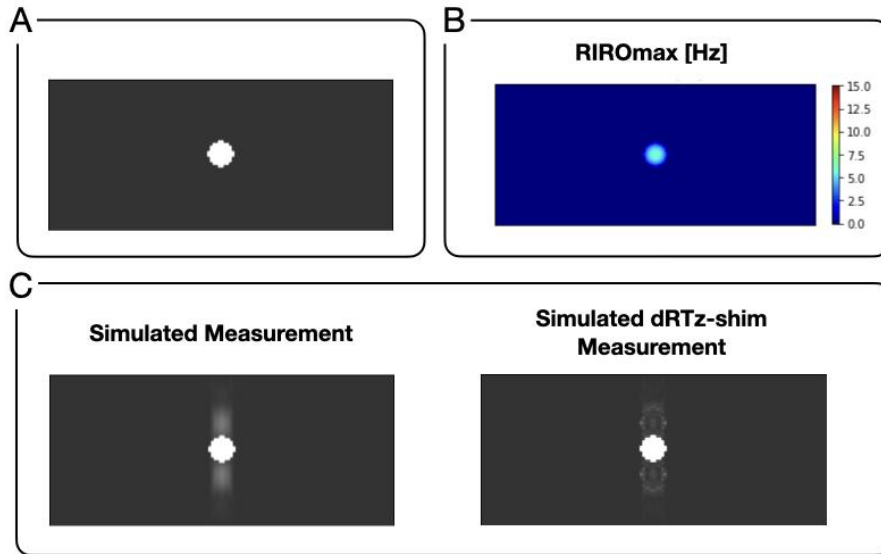


Figure 8: (A) Single-slice simulated cylindrical phantom scan (B) Simulated RIRIOMax distribution (C) Simulated measurements without and with dRTz-shim.

Discussion and Conclusions

The SC is among the most difficult-to-image structures in the body using MRI (21), in part due to the magnetic field inhomogeneities at the interface between bone, intervertebral disks, and cerebrospinal fluid. Among the many requirements for high-quality SC imaging is advanced shimming approaches. In this work, we investigate the feasibility of an approach, called dynamic realtime z-shimming (dRTz-shim), that combines z-shimming with real-time updates from pressure bellows, compensating for both static and time-varying ΔB_0 . To the best of our knowledge, this is the first attempt to correct for respiration-induced resonance offsets (*RIRO*) using the scanner's 1st order shim coils by means of a modified sequence. We have shown evidence, through the use of a pneumatic phantom setup, to support the idea that dRTz-shim may reduce ghosting in MR images. A key requirement for the successful reduction of ghosting using the dRTz-shim approach is in-plane uniformity of *RIRO*. In (22), the authors found minimal in-plane variation of *RIRO* in axial imaging of the occipital lobe at 7 T. Based on our findings, we have determined that the in-plane variability of *RIRO* is too high in the cervical SC region for effective ghosting reduction using dRTz-shim. However, our method may prove to be effective in

brain imaging, or in SC imaging when used in conjunction with reduced FOV acquisition methods, such as 2D RF excitation (23), wherein signal could be suppressed outside of the SC itself, limiting the in-plane $RIR_{O_{max}}$ in the ensuing image to ≈ 1 Hz, which is what we have observed in the SC itself at the C6/C7 level. The implementation of dRTz-shim within a reduced FOV sequence and its use in-vivo will be the purpose of follow-up studies. This could help make MRI techniques that are sensitive to magnetic field inhomogeneities, such as GRE, diffusion-weighted MRI, functional MRI and spectroscopy more feasible in the SC.

Data / Code sharing

The code and data used for simulations are available through a Google Colab page (<https://github.com/evaalonsoortiz/dyn-rt-shim-sim>) where most of the results from the paper can be reproduced on the cloud. Readers can also reproduce our dynamic realtime z-shimming workflow using the *shimming toolbox* that is publicly available: <https://shimming-toolbox.org/>.

Acknowledgments

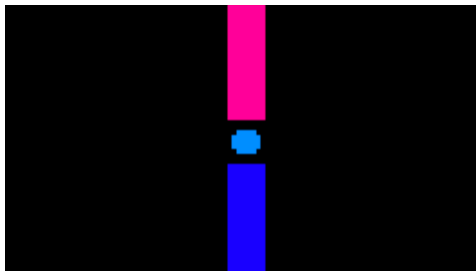
We would like to thank Cyril Tous for his assistance in developing the dynamic realtime z-shimming MGRE sequence and the Functional Neuroimaging Unit for the scanning facilities. This research was undertaken thanks, in part, to funding from the Canada First Research Excellence Fund through a TransMedTech Institute postdoctoral fellowship (Eva Alonso-Ortiz), the Systems, Technologies and Applications for Radiofrequency and Communications (STARaCOM) through a postdoctoral scholarship (Eva Alonso-Ortiz), the Natural Sciences and Engineering Research Council through a postdoctoral fellowship (Eva Alonso-Ortiz), the Courtois Neuromod foundation, the Canada Research Chair in Quantitative Magnetic Resonance Imaging [950-230815], the Canadian Institute of Health Research [CIHR FDN-143263], the Canada Foundation for Innovation [32454, 34824], the Fonds de Recherche du Québec - Santé [28826], the Natural Sciences and Engineering Research Council of Canada [RGPIN-2019-07244], the Canada First Research Excellence Fund (IVADO) and the Quebec BioImaging Network [5886, 35450].

References

1. Finsterbusch J, Eippert F, Büchel C. Single, slice-specific z-shim gradient pulses improve T2*-weighted imaging of the spinal cord. *Neuroimage* 2012;59:2307–2315.
2. Jezzard P, Balaban RS. Correction for geometric distortion in echo planar images from B0 field variations. *Magn. Reson. Med.* 1995;34:65–73.
3. Stockmann JP, Wald LL. In vivo B0 field shimming methods for MRI at 7T. *Neuroimage* 2018;168:71–87.
4. Punchard WFB, Lo K-M, Starewicz PM, Hetherington H. Shim insert for high-field MRI magnets. US Patent 2013.
5. Topfer R, Starewicz P, Lo K-M, et al. A 24-channel shim array for the human spinal cord: Design, evaluation, and application. *Magn. Reson. Med.* 2016;76:1604–1611.
6. Juchem C, Brown PB, Nixon TW, McIntyre S, Rothman DL, de Graaf RA. Multicoil shimming of the mouse brain. *Magn. Reson. Med.* 2011;66:893–900.
7. Blamire AM, Rothman DL, Nixon T. Dynamic shim updating: a new approach towards optimized whole brain shimming. *Magn. Reson. Med.* 1996;36:159–165.
8. Constable RT, Spencer DD. Composite image formation in z-shimmed functional MR imaging. *Magn. Reson. Med.* 1999;42:110–117.
9. Barry RL, Menon RS. Modeling and suppression of respiration-related physiological noise in echo-planar functional magnetic resonance imaging using global and one-dimensional navigator echo correction. *Magn. Reson. Med.* 2005;54:411–418.
10. Pfeuffer J, Van de Moortele P-F, Ugurbil K, Hu X, Glover GH. Correction of physiologically induced global off-resonance effects in dynamic echo-planar and spiral functional imaging. *Magn. Reson. Med.* 2002;47:344–353.
11. Glover GH, Li TQ, Ress D. Image-based method for retrospective correction of physiological motion effects in fMRI: RETROICOR. *Magn. Reson. Med.* 2000;44:162–167.
12. Vannesjo SJ, Clare S, Kasper L, Tracey I, Miller KL. A method for correcting breathing-induced field fluctuations in T2*-weighted spinal cord imaging using a respiratory trace. *Magn. Reson. Med.* 2019;81:3745–3753.
13. van Gelderen P, de Zwart JA, Starewicz P, Hinks RS, Duyn JH. Real-time shimming to compensate for respiration-induced B0 fluctuations. *Magn. Reson. Med.* 2007;57:362–368.
14. Topfer R, Foias A, Stikov N, Cohen-Adad J. Real-time correction of respiration-induced distortions in the human spinal cord using a 24-channel shim array. *Magn. Reson. Med.* 2018;80:935–946.
15. Brown RW, Cheng Y-CN, Mark Haacke E, Thompson MR, Venkatesan R. *Magnetic Resonance Imaging: Physical Principles and Sequence Design.* John Wiley & Sons; 2014.

16. Reeder SB, Atalar E, Bolster BD, McVeigh ER. Quantification and reduction of ghosting artifacts in interleaved echo-planar imaging. *Magn. Reson. Med.* 1997;38:429–439.
17. Morozov D, Rios NL, Duval T, Foias A, Cohen-Adad J. Effect of cardiac-related translational motion in diffusion MRI of the spinal cord. *Magn. Reson. Imaging* 2018;50:119-124.
18. D’Astous A, Topfer R, Cereza G, et al. Shimming-Toolbox: An open-source software package for performing realtime B0 shimming experiments.
19. De Leener B, Lévy S, Dupont SM, et al. SCT: Spinal Cord Toolbox, an open-source software for processing spinal cord MRI data. *Neuroimage* 2017;145:24–43.
20. Jackson E, Bronskill M, Drost D, et al. Tg 1 - Acceptance Testing and Quality Assurance Procedures for Magnetic Resonance Imaging Facilities. American Association of Physicists in Medicine (AAPM); 2010.
21. Martin AR, Aleksanderek I, Cohen-Adad J, et al. Translating state-of-the-art spinal cord MRI techniques to clinical use: A systematic review of clinical studies utilizing DTI, MT, MWF, MRS, and fMRI. *Neuroimage Clin* 2016;10:192–238.
22. Van de Moortele P-F, Pfeuffer J, Glover GH, Ugurbil K, Hu X. Respiration-induced B0 fluctuations and their spatial distribution in the human brain at 7 Tesla. *Magn. Reson. Med.* 2002;47:888–895.
23. Rieseberg S, Frahm J, Finsterbusch J. Two-dimensional spatially-selective RF excitation pulses in echo-planar imaging. *Magn. Reson. Med.* 2002;47:1186–1193.

Supplementary Material



Supplementary Figure S1: Mask used for Percent Signal Ghosting (PSG) calculation for phantom scans. The ROI above the imaged object (see Equation 9) is in pink, the ROI below the imaged object is in dark blue, and the ROI within the imaged object is in light blue.